

Evaluating a Stand-Alone Quantum-Dot Single-Photon Source for Quantum Key Distribution at Telecom Wavelengths

Timm Kupko,¹ Lucas Rickert,¹ Felix Urban,¹ Jan Große,¹ Nicole Srocka,¹ Sven Rodt,¹ Anna Musiał,² Kinga Żołnacz,³ Paweł Mergo,⁴ Kamil Dybka,⁵ Waclaw Urbańczyk,³ Grzegorz Sek,² Sven Burger,⁶ Stephan Reitzenstein,¹ and Tobias Heindel^{1,*}

¹*Institute of Solid State Physics, Technische Universität Berlin, 10623 Berlin, Germany*

²*Department of Experimental Physics, Wrocław University of Science and Technology, 50-370 Wrocław, Poland*

³*Department of Optics and Photonics, Wrocław University of Science and Technology, 50-370 Wrocław, Poland*

⁴*Institute of Chemical Sciences, Maria Curie Skłodowska University, 20-031 Lublin, Poland*

⁵*FibraIn Sp. z o.o., 36-062 Zaczernie, Poland*

⁶*Zuse Institute Berlin, 14195 Berlin, Germany*

Deterministic solid-state quantum light sources are key building blocks in photonic quantum technologies. While several proof-of-principle experiments of quantum communication using such sources have been realized, all of them required bulky setups. Here, we evaluate for the first time the performance of a compact and stand-alone fiber-coupled single-photon source emitting in the telecom O-band (1321 nm) for its application in quantum key distribution (QKD). For this purpose, we developed a compact 19" rack module including a deterministically fiber-coupled quantum dot single-photon source integrated into a Stirling cryocooler, a pulsed diode laser for driving the quantum dot, and a fiber-based spectral filter. We further employed this compact quantum light source in a QKD testbed designed for polarization coding via the BB84 protocol resulting in $g^{(2)}(0) = 0.10 \pm 0.01$ and a raw key rate of up to (4.72 ± 0.13) kHz using an external laser for excitation. In this setting we investigate the achievable performance expected in full implementations of QKD. Using 2D temporal filtering on receiver side, we evaluate optimal parameter settings for different QKD transmission scenarios taking also finite key size effects into account. Using optimized parameter sets for the temporal acceptance time window, we predict a maximal tolerable loss of 23.19 dB. Finally, we compare our results to previous QKD systems using quantum dot single-photon sources. Our study represents an important step forward in the development of fiber-based quantum-secured communication networks exploiting sub-Poissonian quantum light sources.

I. INTRODUCTION

Quantum light sources are building blocks for advanced photonic quantum technologies and quantum communication in particular. Among the several promising species of quantum emitters in the solid-state [1, 2], semiconductor quantum dots (QD) stand out due to the highest reported single photon purity [3, 4] in terms of $g^{(2)}(0)$, high photon indistinguishability and brightness of single- and entangled-photon states [5–7], and their potential for high trigger rates [8, 9]. The advancements of deterministic fabrication technologies had a large impact on these developments - a summary can be found in a recent review article [10]. Furthermore, QD single-photon sources (SPS) have been employed in proof-of-concept QKD experiments [11–13] demonstrating their potential for quantum communication. Until recently, a long-standing drawback of almost all QD-based SPSs was the need for bulky cryotechnology often requiring liquid helium infrastructure. Recently, we resolved this issue by an innovative concept combining fiber-pigtailed deterministically fabricated QD-devices with compact Stirling cryocoolers for stand-alone operation [14–16]. This approach enables one to realize practical QD-SPSs, which

can be operated outside shielded laboratories.

In this work, we report on the first application of a compact stand-alone QD-SPS operating at telecom spectral ranges in experimental tests for BB84-QKD. For this purpose, we developed the most compact stand-alone QD-SPS realized to date. Integrated into a BB84 QKD testbed, we evaluate the performance of our QD-SPS in terms of quantum bit error ratios and achievable key rates also accounting for finite key size effects. Applying 2D temporal filtering of the single-photon pulses [17], we are able to optimize the secret key rates achievable in full implementations for a given loss in the quantum channel.

II. RESULTS

A. QKD Testbed

The QKD testbed developed for the studies in this work is illustrated in Fig. 1(a). On the transmitter side, Alice comprises an optically triggered SPS operating in the telecom O-band. Here, single-photon pulses are generated using a deterministically fabricated QD device, which is directly and permanently coupled to a specialty Ge-doped fiber with NA=0.42. The fiber-pigtailed QD sample is integrated in a linear-piston Stirling cryocooler for operation at 40 K. The QD is optically triggered using either a fiber-coupled diode-laser by Pico-

* Corresponding author: tobias.heindel@tu-berlin.de

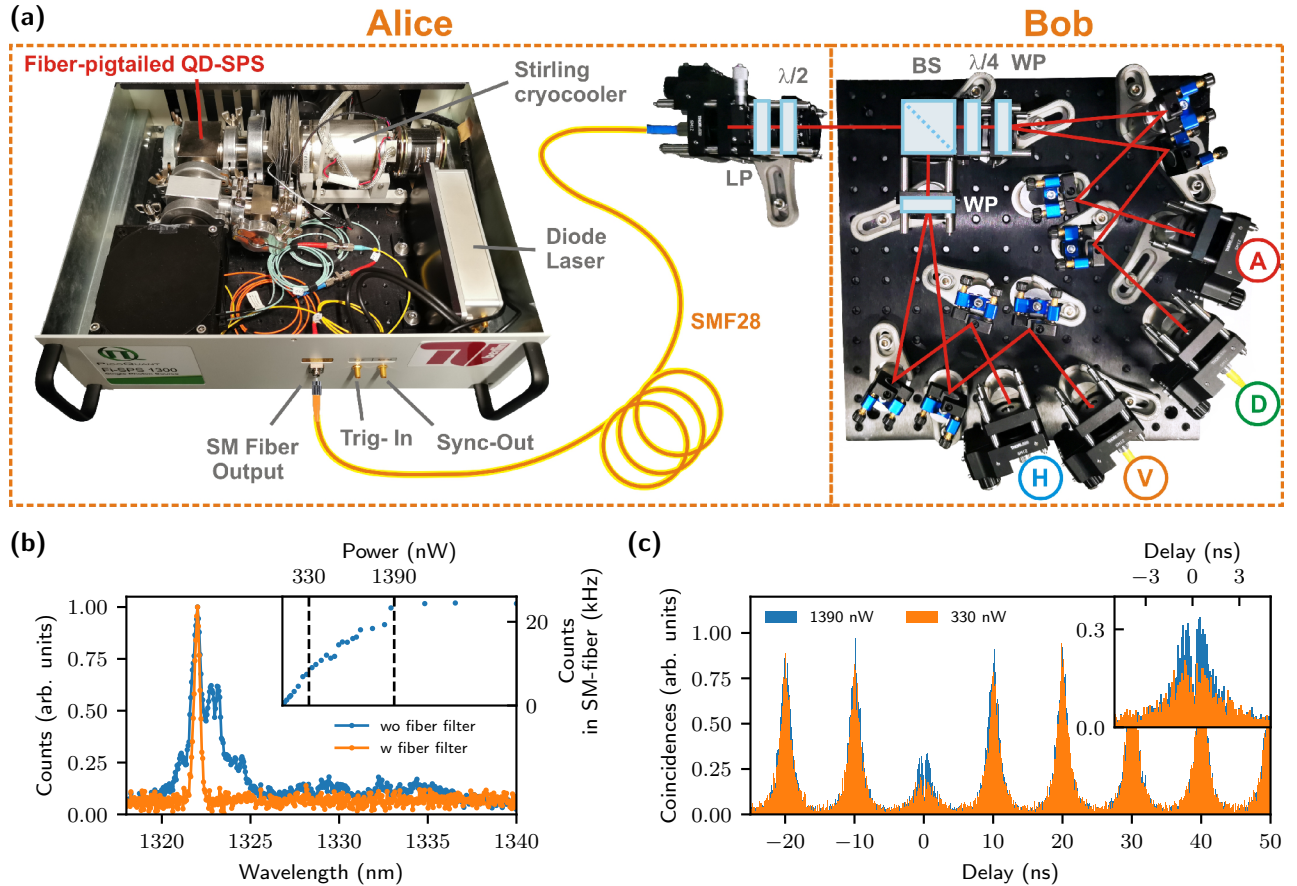


FIG. 1. BB84-QKD testbed using a compact stand-alone quantum dot (QD) single-photon source (SPS) integrated in a 19 inch rack-module and polarization encoding. (a) The transmitter Alice comprises of a deterministically fiber-coupled QD-SPS integrated in a Stirling cryocooler, a pulsed diode-laser for excitation, and a fiber-based spectral filter (not shown in the image). Alice sends pulses with fixed polarization (H, V, D, A) set by a linear polarizer (LP) and a lambda-half ($\lambda/2$) waveplate to Bob. Bob comprises a four-state polarization analyzer realized with a 50:50 beamsplitter (BS), a compensating λ -quarter ($\lambda/4$) waveplate, and two Wollaston-prisms (WP) for spatial separation of orthogonal polarizations. (b) Output spectra of the fiber-coupled SPS with (orange) and without (blue) spectral filtering using a fiber-based bandpass filter set to a center wavelength of 1321 nm (solid lines in the spectra are a guide to the eye). Spectra were recorded at a temperature set-point of the Stirling cryocooler of 40 K. (c) Second-order autocorrelation $g^{(2)}(\tau)$ histogram (100 ps bin width) under pulsed excitation at 785 nm using the internal laser. Depending on the excitation power (see inset), more or less pronounced recapture processes are observed near $\tau = 0$ due to the above-band excitation scheme.

Quant GmbH emitting at 785 nm with variable repetition rate integrated inside the 19" rack module alongside the Stirling cryocooler or an external laser source coupled into a fiber. With a 90/10 fiber coupler the emission is coupled out and the laser is coupled in, respectively. For high-transmission and compact spectral filtering, a fiber-based bandpass filter with adjustable center wavelength is used (full-width at half maximum 0.5 nm) which fits also inside the 19" rack module. For further details see appendix section "Single-Photon Source". We refer to Ref. [16] for details on the SPS device fabrication. Figure 1 (b) shows the output spectrum of the SPS triggered by the integrated diode laser with and without bandpass filter, respectively. The corresponding second-order autocorrelation histogram $g^{(2)}(\tau)$

recorded at the spectrally filtered SPS output using a standard fiber-coupled Hanbury-Brown and Twiss setup and superconducting nanowire single-photon detectors (SNSPDs) (Single Quantum Eos) with a temporal resolution between 35 ps and 100 ps, is shown in Fig. 1 (c) for excitation powers at saturation (1390 nW) and well below saturation (330 nW) of the QD. The extracted integrated antibunching values of $g^{(2)}(0) = 0.49 \pm 0.01$ at saturation and $g^{(2)}(0) = 0.37 \pm 0.02$ at 330 nW indicate single-photon emission. Noteworthy, the suppression of multi-photon emission events is strongly limited by recapture processes (cf. Fig. 1 (c) inset) resulting from the applied above-band excitation scheme. To improve the single-photon purity for QKD tests we applied pulsed (80 MHz) resonant p-shell excitation of the QD in the

following using an external laser tuned to a wavelength of 1247.9 nm which allowed us to achieve $g^{(2)}(0)$ values as low as $g^{(2)}(0) = 0.10 \pm 0.01$.

To evaluate the performance of our stand-alone SPS for applications in quantum communication, we prepare single-photon pulses in four polarization states, required for implementations of the BB84 protocol, using a linear polarizer and a $\lambda/2$ waveplate. The polarization qubits are then sent to the receiver, Bob, in a back-to-back configuration. Although the source is preferably suitable for fiber-based QKD, we use free-space optics for the receiver module instead of fiber optics due to the lower intrinsic QBER, a larger spectral bandwidth, and similar transmission. Bob comprises a 4-state polarization decoder designed for O-band wavelengths, with its four output fibers connected to the SNSPDs. A time-tagging electronic (quTAG, qutools GmbH) is used for registering the events at the detector. Inside Bob, the polarization basis is first passively chosen via a non-polarizing beam-splitter (BS) followed by two Wollaston prisms (WPs) with one of them aligned at an relative angle of 45° . In addition, we use a quarter wave plate in the transmission path to compensate for a slight ellipticity introduced by the BS. For further details see appendix section “Receiver Module”.

B. QKD Performance Evaluation

The most important performance parameter in a QKD system is the secret key rate. In this work we are investigating a practical single-photon source with a finite multi-photon emission probability p_m . The secret key rate for the asymptotic case (i.e., infinite key length) is hence given by [18, 19]

$$S_\infty = S_{\text{sift}} [A(1 - h(e/A)) - f_{\text{EC}}h(e)]. \quad (1)$$

Here, S_{sift} is the sifted key rate, $A = (p_{\text{click}} - p_m)/p_{\text{click}}$ the single-photon detection probability calculated from multi-photon emission probability p_m and overall click probability p_{click} , e is the quantum bit error ratio (QBER), $h(e)$ the binary Shannon-entropy and f_{EC} is the error correction efficiency. For an ideal SPS (i.e., $p_m = 0$) the factor A equals unity, so A is a correction term for realistic SPSs.

First, we investigate the performance of our Bob module which is characterized by its transmission loss and its contribution to the overall QBER. For this purpose, we sequentially prepared single-photon pulses in horizontal (H), vertical (V), diagonal (D), and antidiagonal (A) polarization and recorded the photon arrival time distribution at each of the four detection channels. The resulting experimental data are summarized in Fig. 2 (a) in a 4x4 matrix, where each row corresponds to one input-polarization and columns to the respective detection channel. The expected behavior of the polarization decoder is clearly observed. For a given input-state, almost all photons - where the wrong fraction corresponds

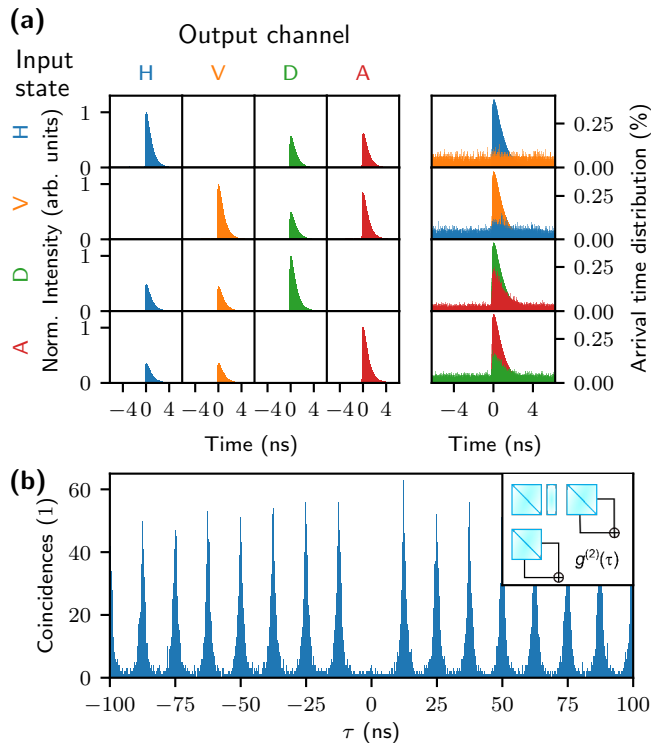


FIG. 2. Characterization of the receiver module Bob using triggered single-photon pulses from Alice as input. (a) Measured photon arrival time distributions at the four detection channels of Bob for single-photon input-polarizations of H, V, D, and A. Measurement data in the left 4x4 matrix are normalized to the maximum of the respective input state. The right panel shows the two data sets for the given input polarization basis (e.g. HH and HV) for each input state normalized to the respective number of events for each channel. This photon arrival probability distribution reveals erroneous detection events due to optical imperfections in Bob. (b) Second-order autocorrelation $g^{(2)}(\tau)$ histogram (50 ps bin width) under pulsed resonant p-shell excitation at 1247.9 nm $g^{(2)}(0) = 0.10 \pm 0.01$. The autocorrelation was obtained by correlating the time-tags recorded at all four detection channels of Bob as shown in the inset.

to the QBER - are detected in the correct channel of the corresponding basis, whereas a probabilistic projection is observed in the conjugate basis. Erroneous detection events at the wrong channel are only visible by plotting the arrival probability distribution for both output channels in a given basis, as depicted in the right panel of Fig. 2 (a). These errors result from the detector dark counts, accumulating to a total of (42 ± 1) Hz at the chosen working point of the SNSPDs (mean detection efficiency -2.2 dB), and optical imperfections. Additional deviations from an ideal setup are due to detection efficiency mismatches between channels. The corresponding contribution to the QBERs extracted from the experimental data are in a range between $\text{QBER}_H = 0.35\%$ and $\text{QBER}_D = 0.82\%$ and are denoted as e_{detector} in the following.

Next, we consider the multi-photon emission probability p_m of our sub-Poissonian quantum light source. This is not as straightforward as in implementations using weak coherent pulses obeying Poissonian statistics. We estimate the upper bound $p_m = \mu^2 g^{(2)}(0)/2$ according to Ref. [20], with μ denoting the mean photon number per pulse. To determine the photon statistics inside the quantum channel of our QKD testbed, we calculated $g^{(2)}(\tau)$ by correlating all time-tags registered at Bobs' four output channels as displayed in Fig. 2 (b) [17]. Here, recapture processes are strongly suppressed compared to the above-band excitation shown in Fig. 1 (c), due to the resonant p-shell excitation of the quantum emitter. In this work we use an external laser for the p-shell excitation. This external laser can be replaced in the future by using a wavelength matched internal laser, a compact tunable ps-lasers [21], or even an on-chip laser [22, 23]. We extract an antibunching value of $g^{(2)}(0) = 0.10 \pm 0.01$ for this measurement by integrating the coincidences over the full repetition period of 12.49 ns. To the best of our knowledge, this corresponds to the lowest antibunching value observed for a compact stand-alone QD-SPS operating at O-band wavelengths. Other fiber-coupled sources [24] achieved similar values ($g^{(2)}(0) = 0.09$) but at lower temperatures using liquid helium infrastructure. Additionally, the record values of $g^{(2)}(0) = 0.027$ for free-space experiments using high-NA microscope objectives both achieved in standard liquid Helium-flow cryostats and using grating spectrometer for spectral filtering [25, 26] are also close. It should also be noted, that the $g^{(2)}(0)$ value achieved here, is currently still limited by the finite laser suppression in the all-fiber-coupled filter configuration of the QD-SPS [16], which can be further improved in the future. Moreover, considering that we neither applied background correction nor fitting routines, this represents a significant improvement compared to previous work with Stirling cryocoolers where a background-corrected value of $g^{(2)}(0) = 0.15$ was reported under above bandgap excitation [16]. Not least, the $g^{(2)}(\tau)$ in the present work indicates a blinking behavior [27] which can be described by the "on-off" model from Ref. [28]. The respective time constants are $\tau_{\text{on}} = (482.3 \pm 2.5)$ ns and $\tau_{\text{off}} = (275.1 \pm 1.0)$ ns yielding a QD "on" state efficiency of 57% reducing the efficiency of our source. It should be noted, that this blinking effect is not a fundamental limit and can possibly be overcome by optimizing the QD growth or embedding QDs in charge tunable devices [29]. In addition, we observe higher photon detection rates of (4.72 ± 0.13) kHz compared to 1.15 kHz in Ref. [16] due to reduced losses in the detection apparatus. From our detection rates and the transmission of the Bob module $\eta_{\text{Bob}} = 0.3$ we can determine the mean photon number per pulse into the quantum channel to be $\mu = 0.0002$. We note here that employing our source in a full implementation would yield a slightly lower μ due to the use of an electro-optical modulator with typical internal losses of about -2 dB. Based on the parameter analysis from our QKD testbed,

	Ref. [11]	Ref. [30]	This Work
Wavelength (nm)	877	1580.5	1321
μ	0.0070	0.0250	0.0002
p_{dc}	1.05e-6	3e-7	5.25e-7
e_{detector}	0.025	0.023	0.010
η_{Bob}	0.24	0.017	0.3
$g^{(2)}(0)$	0.1400	0.0051	0.1000

TABLE I. Relevant parameters to calculate the secret key rates in Fig.4 (b). The parameters for Ref. [11] and Ref. [30] are based on the respective published experimental data. The efficiency η_{Bob} and p_{dc} are lower when applying individual filtering.

the secret key rate expected in a full implementation of QKD can be estimated. To evaluate optimal performance regimes we apply a routine for 2D temporal filtering recently reported by our group in Ref. [17].

As the quantum emitter has a relatively short lifetime (0.9 ns) compared to the pulse repetition period (12.49 ns), we can efficiently reduce the contribution of clicks due to detector noise by reducing the temporal acceptance window. This results in a reduction of the QBER - ideally down to the limit of below 0.4% caused by optical imperfections in the worst channel. Choosing the optimal trade-off between QBER and sifted key material, the secure key can be maximized for a given channel loss. Due to the asymmetric shape of the photon arrival time distribution it is beneficial to vary both the center t_c and the width Δt of the acceptance time window. Figure 3 depicts the estimated asymptotic secret key rate $S(\Delta t, t_c)$ calculated according to Eq. (1) in heat-maps for different loss regimes together with the resulting optimal temporal acceptance window (cf. lower panels and circle in heat-maps) resulting in the largest possible secret key rate. Accounting for the temporal resolution of our experimental setup (convolution of the detector response and the time-tagging device) we used a lower limit for the acceptance time window of 90 ps. Already for a back-to-back transmission (i.e. zero channel loss) discarding some of the sifted key can lead to higher $S(\Delta t, t_c)$ due to the improved signal-to-noise ratio. But not only does the 2D optimization increase $S(\Delta t, t_c)$, it allows also to extend the achievable transmission distance.

C. Finite key size effects

In practical scenarios it is not sufficient to consider only the asymptotic case, as the limited transmission time or transferred data size limits not only the achievable rate at a given distance but also the achievable distance itself. This becomes particular relevant for QKD in free-space optical systems with a relative movement between transmitters and receivers (e.g. airplanes [31], satellites [32–34]), at which stable link-conditions cannot be maintained for a long time. The loss budget of fiber-based connections needs to include finite key size effects espe-

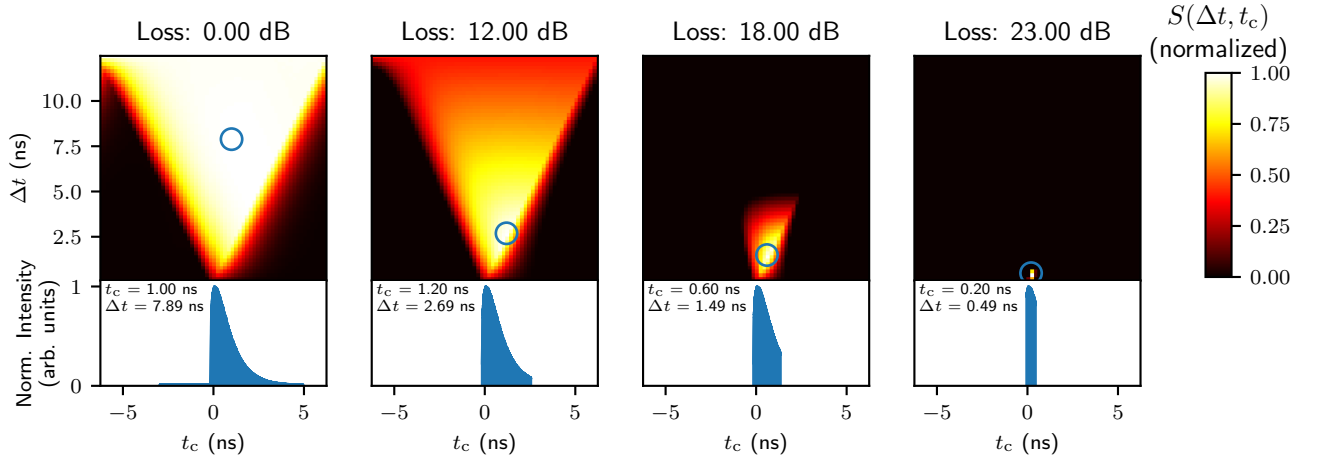


FIG. 3. 2D temporal filtering for optimization of the secret key rate. The data was acquired in a transmission time of 7900 s. Expected secret key rate fraction $S(\Delta t, t_c)$ from Eq. (1) as a function of the temporal width Δt and the center t_c of the acceptance time window. For the analysis the QBER and the sifted key fraction were considered in a two-dimensional parameter space $(\Delta t, t_c)$, while $g^{(2)}(0)$ was fixed to its unfiltered value (cf. discussion in main text). From the parameters at 0 dB transmission losses, three different loss scenarios (12 dB, 18 dB, 23 dB) are simulated. A blue circle marks the optimal parameter sets resulting in a maximal secure key rate. Additionally, the evaluated optimal acceptance time window is depicted in the time-resolved measurements in the lower panels.

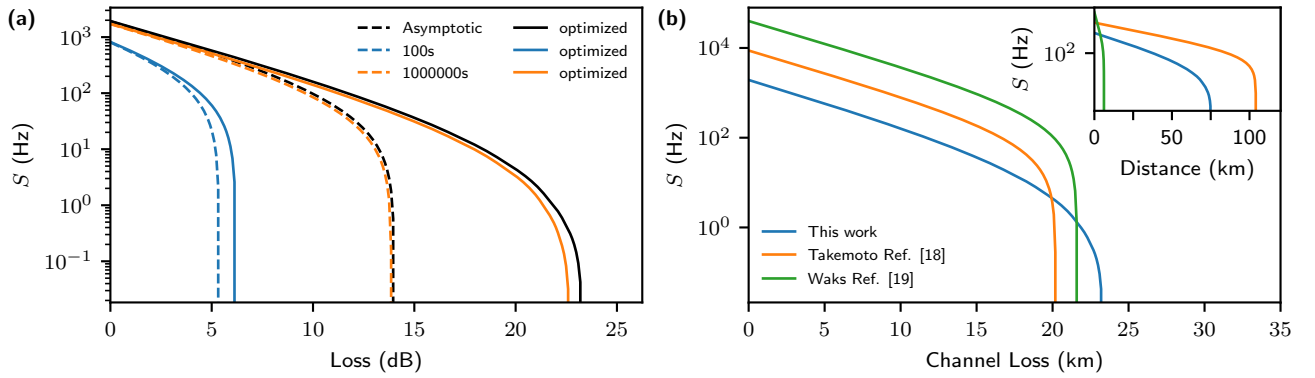


FIG. 4. Rate-loss diagrams considering our experimental data from Fig. 3. (a) Comparison between asymptotic (Eq. (1)) and finite (Eq. (2)) key rate. The secret key rate S in full QKD-implementations is calculated from our experimental parameters. The values without optimizations are depicted with dashed lines, the optimized values with solid lines, respectively. (b) Comparison of our optimized parameter set with previous QD-based QKD implementations for fiber channel. We assume 0.31 dB/km for our source at 1321 nm, for Ref. [30] 0.194 dB/km at 1580.5 nm, and for Ref. [11] 3.5 dB/km at 877 nm.

cially in regimes with high losses and therefore long transmission times. Adapting the finite size key corrections of Ref. [35] the key rate in Eq. (1) is modified:

$$S_{\text{finite}}(N) = nA(1 - h(\tilde{e}/A)) - nf_{\text{EC}}h(e) - \Delta(n). \quad (2)$$

First, one has to take into account that not all of the sifted key S_{sift} can be used for the secret key but a fraction of it has to be discarded for parameter estimation. Out of the sifted events a number of m is taken for parameter estimation and the remaining n bits are used for the key generation. Taking only a finite sample m might lead to deviations between the estimated and the actual error rate. This is taken into consideration by

$$\tilde{e} = e + \sqrt{(\ln(1/\epsilon_{\text{PE}}) + 2 \ln(m+1))/2m} \quad (3)$$

where ϵ_{PE} is the probability for such deviations to occur. Additional finite corrections are subsumed as $\Delta(n)$

$$\Delta(n) = 7n \sqrt{\frac{1}{n} \log_2 \frac{2}{\tilde{e}}} + 2 \log_2 \frac{1}{\epsilon_{\text{PA}}} + \log_2 \frac{2}{\epsilon_{\text{EC}}}, \quad (4)$$

with the overall security parameter $\epsilon = \epsilon_{\text{EC}} + \tilde{e} + \epsilon_{\text{PE}} + \epsilon_{\text{PA}}$ including the failure probabilities for the error correction ϵ_{EC} , the entropy estimation \tilde{e} , the parameter estimation ϵ_{PE} , and the privacy amplification ϵ_{PA} [35].

The rate-loss diagram in Fig. 4 (a) comparatively illustrates the asymptotic and finite-size secret key rates S calculated via Eq. (1) and Eq. (2), respectively, considering our experimentally determined parameters. The maximal tolerable loss for our test-system is limited to

13.96 dB in the non optimized asymptotic case. However, with 2D temporal filtering individually optimized for each loss, one does not only get a slightly higher secret key rate back-to-back but can additionally extend the tolerable losses up to 23.19 dB. In a state-of-the-art single-mode fiber with losses of 0.31 dB/km at 1300 nm this corresponds to a range extension of almost 30 km from 45.0 km to 74.8 km. Taking finite key size effects into account Alice has to send for a minimum transmission time of 18 seconds to yield a positive S in the back-to-back case. Increasing the transmission time by one order of magnitude to 100 seconds would already allow for 6.8 dB of loss in the optimized case. With unpractical transmission times of 1×10^6 seconds one could almost reach the asymptotic case. By comparing the two cases of rather short and long transmission times one can see, that the range extension gained by applying 2D temporal filtering increases with the transmission time.

Finally, we compare our simulated S with previous QKD implementations employing QD based SPSs (Ref. [11], Ref. [30]). For a better comparison we are using the asymptotic rates since those are the ultimate limits for all systems. The parameters used for the comparison are summarized in Tab. I. We assume implementations in SM fiber with losses of 0.31 dB/km in our case, for Ref. [30] 0.194 dB/km, and for Ref. [11] 3.5 dB/km. While the first proof-of-principle implementation by Waks et al. in 2002 achieved a higher $\mu = 0.007$ compared to our present stand-alone device, their wavelength is not ideal for fiber based implementations. Therefore, the achievable distance in optical fiber is relatively small. From all of the three works, our optimized case allows for the highest tolerable losses due to low dark counts and a low intrinsic QBER due to residual optical imperfections (which increases slightly for full implementations with our system due to finite state preparation fidelities of dynamically modulated EOMs). However, the system of Takemoto et al. in Ref. [30] still achieves the highest possible transmission distance due to the low losses in fiber in the telecom C-band. Please note that deviations in the achievable transmission distance compared to the original references are related to the use of slightly different rate equations or p_m and a different f_{EC} . Not least, also the previous implementations cited here might benefit from 2D temporal filtering, which could allow for performance improvements.

III. CONCLUSIONS

We demonstrated the first QKD test experiments employing a compact and stand-alone solid state based SPS for QKD applications. For this purpose, we developed the most compact QD-SPS operating in the telecom O-band reported to date. The source module housed in a 19 inch rack unit comprises a fiber-pigtailed QD integrated into a Stirling cryocooler, and a fiber-based band-pass filter. On receiver side of the QKD testbed, we

employed a 4-state polarization decoder optimized for O-band wavelengths allowing for low intrinsic QBER. Using this testbed, we demonstrated that maximal tolerable losses of 23.19 dB are achievable in full implementations with this system, if optimization routines are applied for a 2D temporal acceptance time window. We further investigated the impact of finite key size effects to the performance of our testbed and compared our results with previous implementations of QKD using QD-SPSs. While already this simple highly-integrated QD-SPS QKD testbed shows comparable or even superior performance (in terms of tolerable losses) compared to previous work, the source efficiency needs to be improved. This could be achieved in future by employing advanced fiber-coupled SPSs based circular Bragg grating cavities and by improving the fiber-coupling efficiency by better mode matching [36]. Progress in the development of compact cryocoolers could also allow for lower operating temperatures. These lower temperatures could in turn reduce not only recapture but could also allow for creation of photons with high indistinguishability. The results reported in our work show prospects for the application of high-performance QD-based quantum light sources in practical quantum network scenarios.

Appendix A: Single-Photon Source

The single-photon source comprises a single InGaAs/GaAs quantum dot which was preselected and deterministically integrated into a monolithic micromesa structure (height 705 nm, diameter 2 μ m) with a distributed Bragg-reflector mirror (nominal 118 nm Al(0.92)Ga(0.08)As, nominal 102 nm GaAs, 15 pairs) on the bottom side for increasing the photon collection efficiency. The design for increased photon collection efficiency was obtained by using numerical simulations [16, 37]. The emission of the InGaAs/GaAs QDs was shifted to the telecom O-band in the epitaxial growth process by using an InGaAs strain-reducing layer. This SPS is coupled to a custom made high-NA (NA=0.42) fiber with a thermally expanded core onto a standard SMF-28e single-mode fiber [38] and integrated into a Stirling cryocooler with a fiber feed-through. The air-cooled Stirling cryocooler allows for cryogen-free operation of the SPS down to 40 K (at 100 W cooling power) while fitting into a 19 inch rack box. A 90/10 fiber coupler is used to optically pump the quantum emitter and collect its emission, which is spectrally filtered using a fiber-coupled band-pass. The performance of the integrated SPS can be enhanced by using quasi-resonant excitation rather than above-band excitation. To this end we also employed an 80 MHz tunable laser system with 2 ps pulsewidth for QKD tests. For the QD line at 1321 nm we used an excitation wavelength of 1247.9 nm. Additionally, we applied polarization suppression to reduce the laser background. The reflections in the compact SPS are mainly due to the use of fiber mating sleeves using physical contact, the us-

age of angled fiber connectors could reduce them further. Additionally, the fibers in the excitation path are all laid out for a 785 nm laser and are therefore multi-mode for the excitation wavelength of 1247.9 nm.

Appendix B: Receiver Module

The receiver module consists of a four-state polarization analyzer with passive basis choice and four SNSPDs. The passive basis choice is realized via a non-polarizing BS with nominal 50:50 splitting ratio. The discrimination of the polarization after the BS is realized with WP which spatially separate two orthogonal polarizations by an angle of 20° . WPs have a higher extinction ratio of up to 1:100,000 compared to polarizing beamsplitters (PBSs) while still having 90% transmission. Instead of using a half-wave plate to rotate incoming diagonal or antidiagonal light onto the prism's axes we rotate one of the WPs by 45° . This still allows for a low-profile of the overall optical setup in contrast to PBSs. We used the transmission arm of the BS for the rotation of the WP since in transmission the depolarization effect of the BS for the D-A basis are smaller. Additionally, a quarter-wave plate is placed in front of the rotated WP in the transmission arm of the BS to reduce the ellipticity introduced by the BS.

The detectors are single-mode fiber (SMF-28) coupled superconducting nanowire SNSPDs optimized for the telecom-O band. To achieve optimal coupling into the fibers there are two mirrors after the WPs for each of the four fiber couplers. The SNSPDs have a polarization dependent efficiency. The polarization discrimination after the WP is advantageous since the polarization of each channel needs only to be compensated once to achieve the maximum efficiency of the detectors.

The overall transmission loss of the polarization decoder η_{Bob} has been experimentally determined to -5.2 dB including optical losses of -3.0 dB and -2.2 dB loss due to the SNSPD's detection efficiency.

Appendix C: Postprocessing

The time-tags recorded at the four ports of the receiver module were evaluated by homemade software. The laser synchronization signal time-tags were only saved if there was a click during the same cycle in one

of the other channels. More details can be found in [17]. The laser repetition rate is slightly above 80 MHz leading to a full temporal time window of 12.49 ns. This slight deviation has an impact in the data evaluation due to the comparatively long blinking time constants. The time-resolved measurements in Fig. 2 (a) are recorded with 1 ps bin width corresponding to the digital resolution of our time-to-digital converter. The time-bin autocorrelation histograms in Fig.1 (c) and Fig.2 (b) use bin-widths of 100 ps and 50 ps, respectively.

ACKNOWLEDGMENTS

We gratefully acknowledge financial support by the German Federal Ministry of Education and Research (BMBF) via project QuSecure (Grant No. 13N14876) within the funding program Photonic Research Germany. The development of the QD-SPS has further been supported by the project FI-SEQUR jointly financed by the European Regional Development Fund (ERDF) of the European Union in the framework of the programme to promote research, innovation, and technologies (Pro FIT) in Germany, and the National Centre for Research and Development in Poland within the 2nd Poland-Berlin Photonics Programme (Grant No. 2/POLBER-2/2016)). S. Rodt and S. Reitzenstein further acknowledge support by the German Science Foundation (DFG) via CRC 787 and S. Burger support via the BMBF-project MODAL/NanoLab (Grant No.: 05M20ZBM). Not least, support by the Polish National Agency for Academic Exchange is gratefully acknowledged.

TK designed and set up the QKD testbed with support by FU, ran the experiments together with LR, and evaluated the experimental data. LR assembled parts of the stand-alone single-photon source, integrated the fiber-pigtailed QD, and operated the source. JG, NS, and S Rodt grew and processed the QD sample under supervision of S Reitzenstein who conceived the QD-SPS development and fabrication. AM and KZ fiber-pigtailed the QD under supervision of WU and GS using the high-NA specialty fiber developed by PM and KD. KD connected the specialty and the standard SM-fiber. SB contributed numerically optimized devices designs for processing the QD sample. TK, LR, and TH wrote the manuscript with input from all authors. TK and LR contributed equally to this work. TH conceived the experiments presented in this work and supervised all efforts on the QKD testbed.

-
- [1] I. Aharonovich, D. Englund, and M. Toth, *Nature Photonics* **10**, 631 (2016).
 - [2] Y. Arakawa and M. J. Holmes, *Applied Physics Reviews* **7**, 021309 (2020).
 - [3] L. Schweickert, K. D. Jöns, K. D. Zeuner, S. F. C. da Silva, H. Huang, T. Lettner, M. Reindl, J. Zichi,

R. Trotta, A. Rastelli, and V. Zwiller, *Applied Physics Letters* **112**, 093106 (2018).

- [4] T. Miyazawa, K. Takemoto, Y. Nambu, S. Miki, T. Yamashita, H. Terai, M. Fujiwara, M. Sasaki, Y. Sakuma, M. Takatsu, T. Yamamoto, and Y. Arakawa, *Applied Physics Letters* **109**, 132106 (2016).

- [5] J. Liu, R. Su, Y. Wei, B. Yao, S. F. C. da Silva, Y. Yu, J. Iles-Smith, K. Srinivasan, A. Rastelli, J. Li, and X. Wang, *Nature Nanotechnology* **14**, 586 (2019).
- [6] H. Wang, H. Hu, T.-H. Chung, J. Qin, X. Yang, J.-P. Li, R.-Z. Liu, H.-S. Zhong, Y.-M. He, X. Ding, Y.-H. Deng, Q. Dai, Y.-H. Huo, S. Höfling, C.-Y. Lu, and J.-W. Pan, *Physical Review Letters* **122** (2019).
- [7] N. Tomm, A. Javadi, N. O. Antoniadis, D. Najer, M. C. Löbl, A. R. Korsch, R. Schott, S. R. Valentin, A. D. Wieck, A. Ludwig, and R. J. Warburton, *Nature Nanotechnology* **16**, 399 (2021).
- [8] A. Schlehahn, A. Thoma, P. Munnely, M. Kamp, S. Höfling, T. Heindel, C. Schneider, and S. Reitzenstein, *APL Photonics* **1**, 011301 (2016).
- [9] G. Shooter, Z.-H. Xiang, J. R. A. Müller, J. Skiba-Szymanska, J. Huwer, J. Griffiths, T. Mitchell, M. Anderson, T. Müller, A. B. Krysa, R. M. Stevenson, J. Hefernan, D. A. Ritchie, and A. J. Shields, *Optics Express* **28**, 36838 (2020).
- [10] S. Rodt, S. Reitzenstein, and T. Heindel, *Journal of Physics: Condensed Matter* **32**, 153003 (2020).
- [11] E. Waks, K. Inoue, C. Santori, D. Fattal, J. Vuckovic, G. S. Solomon, and Y. Yamamoto, *Nature* **420**, 762 (2002).
- [12] T. Heindel, C. A. Kessler, M. Rau, C. Schneider, M. Fürst, F. Hargart, W.-M. Schulz, M. Eichfelder, R. Roßbach, S. Nauerth, M. Lermer, H. Weier, M. Jetter, M. Kamp, S. Reitzenstein, S. Höfling, P. Michler, H. Weinfurter, and A. Forchel, *New Journal of Physics* **14**, 083001 (2012).
- [13] M. Rau, T. Heindel, S. Unsleber, T. Braun, J. Fischer, S. Frick, S. Nauerth, C. Schneider, G. Vest, S. Reitzenstein, M. Kamp, A. Forchel, S. Höfling, and H. Weinfurter, *New Journal of Physics* **16**, 043003 (2014).
- [14] A. Schlehahn, L. Krüger, M. Gschrey, J.-H. Schulze, S. Rodt, A. Strittmatter, T. Heindel, and S. Reitzenstein, *Review of Scientific Instruments* **86**, 013113 (2015).
- [15] A. Schlehahn, S. Fischbach, R. Schmidt, A. Kaganskiy, A. Strittmatter, S. Rodt, T. Heindel, and S. Reitzenstein, *Scientific Reports* **8** (2018).
- [16] A. Musiał, K. Żołnacz, N. Srocka, O. Kravets, J. Große, J. Olszewski, K. Poturaj, G. Wójcik, P. Mergo, K. Dybka, M. Dyrkacz, M. Dłubek, K. Lauritsen, A. Bültner, P.-I. Schneider, L. Zschiedrich, S. Burger, S. Rodt, W. Urbaczyk, G. Sęk, and S. Reitzenstein, *Advanced Quantum Technologies* **3**, 2000018 (2020).
- [17] T. Kupko, M. von Helversen, L. Rickert, J.-H. Schulze, A. Strittmatter, M. Gschrey, S. Rodt, S. Reitzenstein, and T. Heindel, *npj Quantum Information* **6** (2020).
- [18] D. Gottesman, H.-K. Lo, N. Lütkenhaus, and J. Preskill, *Quantum Info. Comput.* **4**, 325–360 (2004).
- [19] P. Chaiwongkhot, S. Sajeed, L. Lydersen, and V. Makarov, *Quantum Science and Technology* **2**, 044003 (2017).
- [20] E. Waks, C. Santori, and Y. Yamamoto, *Physical Review A* **66**, 042315 (2002).
- [21] A. C. Dada, T. S. Santana, R. N. E. Malein, A. Koutroumanis, Y. Ma, J. M. Zajac, J. Y. Lim, J. D. Song, and B. D. Gerardot, *Optica* **3**, 493 (2016).
- [22] P. Munnely, T. Heindel, A. Thoma, M. Kamp, S. Höfling, C. Schneider, and S. Reitzenstein, *ACS Photonics* **4**, 790 (2017).
- [23] Z.-H. Xiang, J. Huwer, J. Skiba-Szymanska, R. M. Stevenson, D. J. P. Ellis, I. Farrer, M. B. Ward, D. A. Ritchie, and A. J. Shields, *Communications Physics* **3** (2020).
- [24] C.-M. Lee, M. A. Buyukkaya, S. Aghaeimeibodi, A. Karasahin, C. J. K. Richardson, and E. Waks, *Applied Physics Letters* **114**, 171101 (2019).
- [25] Ł. Dusanowski, P. Holewa, A. Maryński, A. Musiał, T. Heuser, N. Srocka, D. Quandt, A. Strittmatter, S. Rodt, J. Misiewicz, S. Reitzenstein, and G. Sęk, *Optics Express* **25**, 31122 (2017).
- [26] N. Srocka, P. Mrowiński, J. Große, M. von Helversen, T. Heindel, S. Rodt, and S. Reitzenstein, *Applied Physics Letters* **116**, 231104 (2020).
- [27] J.-P. Jahn, M. Munsch, L. Béguin, A. V. Kuhlmann, M. Renggli, Y. Huo, F. Ding, R. Trotta, M. Reindl, O. G. Schmidt, A. Rastelli, P. Treutlein, and R. J. Warburton, *Physical Review B* **92** (2015).
- [28] C. Santori, M. Pelton, G. Solomon, Y. Dale, and Y. Yamamoto, *Physical Review Letters* **86**, 1502 (2001).
- [29] L. Zhai, M. C. Löbl, G. N. Nguyen, J. Ritzmann, A. Javadi, C. Spinnler, A. D. Wieck, A. Ludwig, and R. J. Warburton, *Nature Communications* **11** (2020).
- [30] K. Takemoto, Y. Nambu, T. Miyazawa, Y. Sakuma, T. Yamamoto, S. Yorozu, and Y. Arakawa, *Scientific Reports* **5** (2015).
- [31] S. Nauerth, F. Moll, M. Rau, C. Fuchs, J. Horwath, S. Frick, and H. Weinfurter, *Nature Photonics* **7**, 382 (2013).
- [32] S.-K. Liao, W.-Q. Cai, W.-Y. Liu, L. Zhang, Y. Li, J.-G. Ren, J. Yin, Q. Shen, Y. Cao, Z.-P. Li, F.-Z. Li, X.-W. Chen, L.-H. Sun, J.-J. Jia, J.-C. Wu, X.-J. Jiang, J.-F. Wang, Y.-M. Huang, Q. Wang, Y.-L. Zhou, L. Deng, T. Xi, L. Ma, T. Hu, Q. Zhang, Y.-A. Chen, N.-L. Liu, X.-B. Wang, Z.-C. Zhu, C.-Y. Lu, R. Shu, C.-Z. Peng, J.-Y. Wang, and J.-W. Pan, *Nature* **549**, 43 (2017).
- [33] J. Yin, Y. Cao, Y.-H. Li, J.-G. Ren, S.-K. Liao, L. Zhang, W.-Q. Cai, W.-Y. Liu, B. Li, H. Dai, M. Li, Y.-M. Huang, L. Deng, L. Li, Q. Zhang, N.-L. Liu, Y.-A. Chen, C.-Y. Lu, R. Shu, C.-Z. Peng, J.-Y. Wang, and J.-W. Pan, *Physical Review Letters* **119** (2017).
- [34] J. Yin, Y.-H. Li, S.-K. Liao, M. Yang, Y. Cao, L. Zhang, J.-G. Ren, W.-Q. Cai, W.-Y. Liu, S.-L. Li, R. Shu, Y.-M. Huang, L. Deng, L. Li, Q. Zhang, N.-L. Liu, Y.-A. Chen, C.-Y. Lu, X.-B. Wang, F. Xu, J.-Y. Wang, C.-Z. Peng, A. K. Ekert, and J.-W. Pan, *Nature* **582**, 501 (2020).
- [35] R. Y. Q. Cai and V. Scarani, *New Journal of Physics* **11**, 045024 (2009).
- [36] L. Rickert, T. Kupko, S. Rodt, S. Reitzenstein, and T. Heindel, *Optics Express* **27**, 36824 (2019).
- [37] P.-I. Schneider, N. Srocka, S. Rodt, L. Zschiedrich, S. Reitzenstein, and S. Burger, *Optics Express* **26**, 8479 (2018).
- [38] K. Żołnacz, A. Musiał, N. Srocka, J. Große, M. J. Schlöisinger, P.-I. Schneider, O. Kravets, M. Mikulicz, J. Olszewski, K. Poturaj, G. Wójcik, P. Mergo, K. Dybka, M. Dyrkacz, M. Dłubek, S. Rodt, S. Burger, L. Zschiedrich, G. Sęk, S. Reitzenstein, and W. Urbaczyk, *Optics Express* **27**, 26772 (2019).